RSC Advances

PAPER

View Article Online
View Journal | View Issue

Cite this: *RSC Adv.*, 2026, **16**, 21740

Semiconducting SnO_2 nanoparticles for surface-enhanced Raman scattering applications

P. Surya Lakshmi,†[a] B. Mohanarao,†[a] P. Babuji,[a] P. V. Prakash Madduri,[b] L. Jyothi,[c] G. Krishna Podagatlapalli,[a] K. H. Chae,[d] G. S. Chang[e] and V. Saikiran *[a]

Received 30th October 2025
Accepted 23rd March 2026

DOI: 10.1039/d5ra08335d

rsc.li/rsc-advances

This study reports the synthesis of phase-pure SnO_2 nanoparticles using a sol–gel-assisted method and thermal annealing at 800 and 900 °C to optimize their structural and surface properties for non-plasmonic semiconductor-based surface-enhanced Raman scattering (SERS) applications. Comprehensive characterization using X-ray diffraction with Rietveld refinement, high-resolution electron microscopy, and X-ray photo electron spectroscopy confirmed the enhanced crystallinity, spherical morphology, and controlled generation of oxygen vacancies, particularly when annealed at 800 °C. These vacancies were found to play a critical role in facilitating charge transfer, which is the dominant enhancement mechanism in semiconductor-based SERS. Raman spectroscopy verified phonon activation and lattice coherence in post-annealed SnO_2 nanoparticles, while SERS using Nile blue as the analyte demonstrated strong signal enhancement with an estimated enhancement factor of 3.95×10^3 and a detection limit down to 10^{-6} mol L^{-1}. The substrate exhibited high spectral reproducibility and minimal fluorescence interference, even at low analyte concentrations. Notably, this performance was achieved without the use of noble metals or dopants, highlighting the effectiveness of defect engineering *via* thermal treatment. These findings establish thermally optimized SnO_2 as a robust, scalable, and cost-effective SERS platform, offering promising potential for chemical and biosensing applications.

1. Introduction

Surface-enhanced Raman scattering (SERS) has significantly advanced analytical and materials sciences by enabling ultra-sensitive, non-destructive, and label-free molecular detection across diverse applications, including biosensors, environmental monitoring, food safety, and clinical diagnostics.[1–3] Traditionally, the remarkable enhancement of Raman signals in SERS has been attributed to plasmonic nanostructures, typically composed of noble metals, such as Au, Ag, and Cu, which exhibit strong localized surface plasmon resonances upon optical excitation.[4] This enhancement primarily arises from the intense electromagnetic fields concentrated near the surface of metal nanostructures, creating "hot spots" that amplify the Raman signals of nearby molecules by several orders of magnitude. Despite these remarkable properties, plasmonic SERS materials suffer from numerous drawbacks that limit their scalability and applications.[5] The fabrication of plasmonic nanostructures typically involves sophisticated, multi-step processes and expensive raw materials.[6] Furthermore, plasmonic nanostructures are prone to oxidation, agglomeration, and poor reproducibility under ambient conditions, compromising their stability and long-term performance.[7] Due to these issues with metal-based SERS, particularly where large-scale production and cost-efficiency are critical, semiconducting-based SERS is emerging as an alternative method. To address these limitations, semiconductor materials, particularly metal oxides, have emerged as promising, cost-effective alternatives to plasmonic SERS-active materials.[8–11] Among them, tin dioxide (SnO_2), a wide bandgap n-type semiconductor, has demonstrated considerable potential due to its low cost, strong stability, non-toxic nature, and rich surface defect structures.[12,13] Additionally, SnO_2 nanostructures can be synthesized with controlled morphologies and crystallite sizes using simple, scalable methods, making them appealing candidates for next-generation SERS platforms.[14–16]

Unlike plasmonic materials, the enhancement mechanisms in semiconductor-based SERS are primarily governed by charge transfer (CT) and defect-assisted effects.[17] In metal oxides,

[a]*Department of Physics, School of Sciences, GITAM Deemed to be University, Visakhapatnam, 530045, India. E-mail: svadaval@gitam.edu; saivadavalli@gmail.com*

[b]*Department of Sciences, Indian Institute of Information Technology Design and Manufacturing Kurnool, Kurnool 518008, Andhra Pradesh, India*

[c]*School of Physics, University of Hyderabad, Hyderabad 500046, India*

[d]*Advanced Analysis Center, Korea Institute of Science and Technology, Seoul 02792, Republic of Korea*

[e]*Department of Physics and Engineering Physics, University of Saskatchewan, Saskatoon, SK S7N5E2, Canada*

† Equal contribution.

photo-induced electron transfer between the semiconductor active material and analyte molecule, along with surface defects such as oxygen vacancies, plays a crucial role in SERS signal amplification.[18] The morphology and crystalline properties of the semiconductor, including particle size, surface area, defect density, and exposed crystal planes, profoundly influence the density of the available sites for molecule adsorption and CT efficiency.[19] This is particularly pronounced in SnO_2 nanoparticles (NPs), where the abundant surface defects and under-coordinated sites create numerous localized states within the bandgap, enhancing their interaction with analyte molecules.[20] Furthermore, the dimensions and morphology of the SnO_2 NPs affect light absorption, carrier recombination, and photo-induced charges, all of which contribute to the SERS performance.[21]

The application of SnO_2 NPs as an SERS-active material is particularly promising for the sensitive and selective detection of small molecules with analytical and clinical significance, which strongly depends on their interaction with the SERS active surface. The defects and oxygen vacancies present enable effective signal amplification.[22] Therefore, tailoring the morphology, crystallite size, and defect structures of semiconductor NPs to optimize their SERS activity holds great potential for developing high-sensitivity biosensors and analytical platforms.[23] It is equally important to understand the fundamental enhancement mechanisms to improve the material properties and expand their applicability to a broader range of small molecules in healthcare, environmental monitoring, and food safety diagnostics.[24] Over the past few years, SnO_2 nanomaterials (NPs, nanotubes, nanoribbons, *etc.*) have been synthesized using various methods, such as electrochemical synthesis,[25] chemical vapour deposition,[26,27] solution phase growth,[28] and sputtering.[29] Additionally, many nanocomposite materials are prepared using SnO_2, carbon nanotubes and other oxides.[30–32] In general, all these methods follow the synthesis of SnO_2 NPs and are used for sensing and other applications. SERS-based applications were not explored with SnO_2 NPs, which possess more oxygen-related defects and vacancies suitable for CT-based SERS enhancements.

The present study investigates the synthesis of SnO_2 semiconducting oxide NPs and their utilization as SERS-active materials, focusing on their synthesis, structural characterization, defect states, and enhancement mechanisms for SERS. It examines how sample preparation conditions influence morphology, crystallite size, and defect formation and how these factors collectively affect the SERS performance. Ultimately, this study underscores the potential of SnO_2 NPs as scalable, chemically robust, and cost-effective platforms for label-free and non-invasive sensing applications.

2. Experimental details

2.1 Materials and reagents

To prepare SnO_2 NPs, tin chloride ($SnCl_4$) was used as the precursor, and an ammonia solution (NH_4OH) served as the precipitating agent. All chemicals were of analytical grade and used without further purification. Distilled water was used throughout the synthesis process.

2.2 Synthesis of SnO_2 nanoparticles

SnO_2 NPs were synthesized using a sol–gel-assisted precipitation method under ambient conditions. Initially, 0.5 mL of $SnCl_4$ was dissolved in 43.37 mL of distilled water under vigorous stirring to obtain a clear 0.1 M solution. The solution was sonicated for 40 minutes using a bath sonicator to disperse any precursor clusters and promote homogenous nucleation. Following complete dissolution, NH_4OH was added dropwise to the solution under continuous stirring at 400 rpm and was maintained at 100 °C. The addition continued until a persistent white, cloudy precipitate was formed, indicating complete precipitation. The pH was adjusted accordingly during this process to ensure complete conversion. After precipitation, the mixture was stirred for an additional 20 minutes to facilitate homogenous particle formation. The resulting suspension was sonicated again for 40 minutes to break up the agglomerates and then left undisturbed for 12 hours to allow for sedimentation. The sediments were collected by vacuum filtration, thoroughly washed with distilled water and acetone to remove impurities and residual ions, and dried in a hot air oven at 100 °C for 2 hours. Fig. S1 illustrates the sol–gel-assisted precipitation synthesis route.

2.3 Post-annealing treatment

The as-prepared SnO_2 powder is tested using thermogravimetric analysis (TGA) in a N_2 environment using equipment model TGA-DSC Hitachi STA 7300. The plot is shown in the SI (Fig. S2). From this figure, it is observed that at initial temperatures in the range (0 to 200 °C), the weight loss is sharp, and this indicates that the solvents are reduced and surface hydroxy groups are removed from the initially formed as-prepared SnO_2 products. With an increase in temperature, the weight loss is moderate, and the SnO_2 crystalline phase is observed. At high temperatures, SnO_2 is observed to be more stable and suitable for the grain growth of SnO_2 NPs. Additionally, previously reported synthesis of annealing temperatures suggests that temperatures beyond 700 °C are more suitable for phase stable SnO_2 NP synthesis.[25,28] To investigate the effects of thermal treatment on the structure and physical properties of SnO_2 NPs, the dried powders were divided into three batches:

- A1: pristine (as-prepared) samples without further treatment.
- A2: samples annealed at 800 °C for 2 hours in a tubular furnace.
- A3: samples annealed at 900 °C for 2 hours under identical conditions.

All the annealed samples were cooled naturally to room temperature.

2.4 Sample characterization

The structural properties of SnO_2 NPs were investigated using X-ray diffraction (XRD) with Cu-Kα radiation ($\lambda = 0.15406$ nm) (model: Bruker D8) over a 2θ range of 20–80° at a scanning rate

of 0.02° s^{-1}. Crystallite sizes were estimated using the Halder–Wagner approximation.[33–35] The morphology and crystallite size were examined using field-emission scanning electron microscopy (FESEM) (instrument model: Carl ZEISS Ultra55) and transmission electron microscopy (TEM) (instrument model: FEI Technai F20). X-ray photoelectron spectroscopy (XPS) (instrument model: Thermo Scientific UK Kα source) was employed to determine the chemical composition and oxidation states. Defect states were further investigated using near-edge X-ray absorption fine structure (NEXAFS) spectroscopy. O K-edge NEXAFS spectra were recorded at the 10D HR XAS KIST beamline of the Pohang Light Source in the Republic of Korea. All NEXAFS spectra were measured in the total electron yield (TEY) mode. The spectra were intensity-normalized to the incoming photon flux, as recorded by an Au mesh. The detailed procedures for data acquisition, calibration, and normalization are described elsewhere.[36] Raman and SERS measurements were conducted to assess the enhancement mechanisms and sensor properties. Raman measurements were performed using the HR 800 Horiba Jobin Yvon spectrometer with an excitation wavelength of 633 nm.

2.5 SERS measurements

For SERS measurements, SnO_2 NPs were first prepared as a film on a Si substrate by dispersing SnO_2 NP (10 mg) powder in a suitable amount of isopropanol, and then the solution was ultrasonicated for 10–20 min to avoid agglomeration. Subsequently, the solution is deposited on Si substrates using the spin coating method to obtain a uniform film (~40 μL volume of the SnO_2 NP solution is used at 2000 rpm for 35 s). The films were dried in an oven at 70 °C overnight and used as SERS substrates. For SERS signal analysis, a WITec alpha300 modular confocal Raman microscope with an excitation wavelength of 532 nm is used. The analyte solution was prepared by sequentially diluting the stock solutions in acetone. ~10 μL of Nile blue (NB) analyte solution at various concentrations was drop-cast onto the substrate prepared with SnO_2 NPs and dried under ambient conditions prior to SERS measurements. To prevent photo thermal damage, the laser power was maintained at ~5% during data acquisition.

3. Results and discussion

The powder XRD patterns of the synthesized SnO_2 NPs are presented in Fig. 1(A), providing crucial insights into their structural evolution under thermal treatment and laying the foundation for understanding their optical and SERS characteristics. All three samples, A1 (as prepared), A2 (annealed at 800 °C), and A3 (annealed at 900 °C), exhibit diffraction peaks consistent with the tetragonal rutile phase of SnO_2 (space group: $P4_2/mnm$, JCPDS No. 41-1445). Prominent diffraction peaks at $2\theta \approx 26.6°$, 33.9°, 37.9°, 51.7°, and 65.9° due to (110), (101), (200), (211), and (301) Bragg reflection, respectively, confirm phase purity with no detectable secondary phases even after high-temperature annealing.

The XRD profile of the as-prepared sample (A1) shows broad and low-intensity peaks, indicating ultra-small crystallite sizes and significant microstrain, which is typical of sol–gel or hydrothermally synthesized oxide NPs.[37] Upon annealing at 800 °C (A2) and 900 °C (A3), the diffraction peaks become sharper and more intense, while the full width at half maximum (FWHM) decreases. This reflects enhanced crystallinity, grain growth, and a reduced defect concentration. This trend is consistent with previous studies on sol–gel-derived SnO_2, where post-annealing leads to recrystallization, strain relaxation, and the growth of energetically favourable crystal facets.[38] More importantly, this grain growth alters the surface-to-volume ratio, electronic structure, and oxygen vacancy dynamics, factors that are central to SERS performance. At the atomic scale, thermal energy promotes lattice rearrangement, which reduces local defects and compressive stress, resulting in more coherent SnO_6 octahedra. However, the complete elimination of defects is neither observed nor desirable. Annealing at 800 °C appears to provide an optimal balance between improved crystallinity and the retention of beneficial oxygen vacancies, which are known to facilitate CT processes in non-plasmonic SERS substrates.[39]

In the context of SERS, structural refinement by post-annealing plays a dual role: it ensures a stable scaffold for molecular adsorption and preserves localized defect domains that support electron–hole separation and transfer. Previous studies on defect-engineered oxides, such as WO_3 and TiO_2, support this paradigm, demonstrating that moderate structural disorder coupled with crystalline coherence enhances analyte–substrate interactions.[40,41] Moreover, comparative analyses with Ag or Fe-doped SnO_2 systems reveal that crystallite size alone does not dictate SERS activity.[42,43] Instead, it is the interplay between particle size, concentration of oxygen vacancy, and surface chemistry that determines enhancement. Among the samples studied, A2 (annealed at 800 °C) appears to achieve this delicate balance most effectively.

Finally, the absence of extraneous peaks or phase segregation in any XRD profiles confirms the homogeneity of the synthesized materials, a key requirement for reproducible SERS sensing. Variations in crystallinity or impurity content are known to cause signal fluctuations and batch-to-batch inconsistency, which remain major drawbacks in plasmonic SERS platforms. Table 1 summarizes the crystallite size and lattice strain of SnO_2 NPs after annealing.

Rietveld refinement of the XRD pattern provides definitive structural validation in the annealed SnO_2 NPs (Fig. 1(B)). The refined model shows excellent agreement between the experimental and calculated patterns, as evidenced by the close overlap of Bragg profiles and the minimal residuals. This confirms the presence of a long-range crystalline order and suggests minimal instrumental or microstructural distortions. The crystallite size and strain can be determined using average size-strain (ASS) plots, which are constructed using the Halder–Wagner (HW) approximation based on the Rietveld refinement of the XRD patterns.[34] Crystallite sizes, computed using the ASS plots [Fig. 1(C)] for A2 and A3, indicate that crystallite size increases from 13 (±2) nm (A2) to 19 (±2) nm (A3), signifying

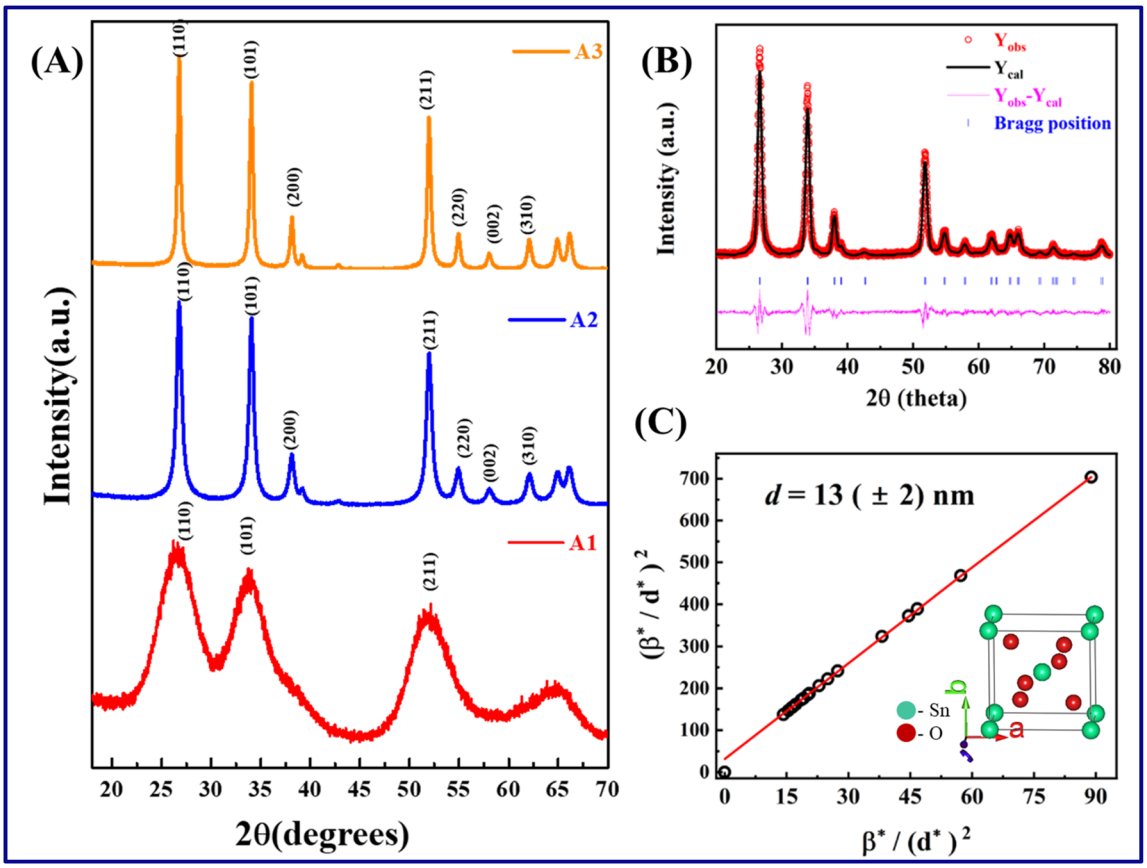

Fig. 1 (A) XRD patterns of the as-prepared (A1) and post-annealed (A2 and A3) SnO_2 NPs, showing peak sharpening and crystallite growth with annealing, (B) Rietveld-refined XRD pattern confirming the tetragonal rutile structure of SnO_2 for A2, and (C) average size-strain Halder–Wagner plot to determine the volume-weighted mean crystallite size (d) for A2. Here, $\beta^*_{hkl} = \frac{\beta_{hkl}\cos(\theta)}{\lambda}$, $d^*_{hkl} = \frac{2d_{hkl}\sin(\theta)}{\lambda}$, β_{hkl} and d_{hkl} represents the broadening of the *hkl* plane and the corresponding crystallite size from the *hkl* plane, respectively. Inset of (C) shows the visualized refined unit cell of SnO_2.

a thermally activated Ostwald ripening process. As expected, an increase in crystallite size reduces lattice strain. The obtained lattice constants $a = b = 4.7376$ Å and $c = 3.1867$ Å are in excellent agreement with the reported values for bulk tetragonal rutile SnO_2, demonstrating the preservation of crystallographic integrity even after high-temperature annealing.[44] The inset of (C) indicates the visualized refined unit cell of SnO_2 obtained from VESTA. Table S1 presents the parameters obtained from Rietveld refinement. This structural stability is important for maintaining consistent surface-active sites, which are essential for reproducible SERS sensing. In contrast, plasmonic materials, like Ag or Cu NPs, often suffer from oxidation, sintering, or phase instability under similar thermal conditions. Notably, the refinement shows no sign of lattice splitting, peak asymmetry, or intensity anomalies that would indicate the presence of sub-phases, such as SnO or Sn_3O_4. The absence of these intermediate oxide phases is critical, as they possess distinct electronic and chemical properties that can disrupt uniform CT pathways and compromise SERS signal consistency. This structural purity enhances the reliability of molecule–substrate interactions, particularly in systems where

Table 1 Crystallite size and lattice strain of SnO_2 NPs after annealing

Sample name	Crystallite size (nm)	Lattice parameters (Å)	Lattice strain	Dislocation density (10^{15} m^{-2})
A1	—	$a = b = 4.730$ $c = 3.2060$	3.9×10^{-2}	—
A2	13 ± 2	$a = b = 4.7376$ $c = 3.1867$	11.18×10^{-4}	5.92
A3	19 ± 2	$a = b = 4.7173$ $c = 3.1757$	9.11×10^{-5}	2.77

defect-mediated CT is the dominant enhancement mechanism.[45]

Although the lattice parameters remain within the bulk range, subtle variations in unit cell volume may reflect oxygen non-stoichiometry or strain effects induced by point defects. In SnO_2 systems, even trace concentrations of oxygen vacancies can lead to measurable lattice distortions due to changes in electrostatic repulsion and local relaxation of the Sn–O framework. These vacancies, particularly when located near the surface, play a direct role in mediating CT between the substrate and adsorbed analytes, an essential process in non-plasmonic SERS.[46]

The structural order revealed by Rietveld refinement also contributes to a uniform electric field distribution across the substrate, which is vital for reproducible SERS signals. Prior studies on TiO_2- and ZnO-based SERS platforms have shown that even minor phase inhomogeneities can localize electric fields or disrupt energy alignment at the semiconductor–molecule interface, thereby reducing the effective cross-section for Raman enhancement.[45] In this context, the phase-pure, single-crystalline domains confirmed using refinement minimize such inconsistencies and optimize analyte interaction zones.

It is also worth noting that while the refinement confirms crystallographic uniformity, it does not rule out the presence of point defects, such as oxygen vacancies, which are, in fact, desirable in semiconductor-based SERS. This makes Rietveld refinement a complementary tool: it validates the structural framework while encouraging further defect-specific investigations through spectroscopic techniques, such as XPS and NEXAFS. In this study, these methods collectively confirm the presence of such defects in a controlled and beneficial form.

Additionally, the narrow FWHM of the Bragg peaks, accurately fitted during refinement, indicates low dislocation density, a microstructural feature that reduces carrier scattering and enhances surface reactivity. In summary, Rietveld refinement confirms that the annealed SnO_2 NPs are structurally robust, phase-pure, and highly crystalline, making them ideal candidates for CT-dominated SERS applications. This result is further supported by consistent results from electron microscopy, surface spectroscopy, and functional Raman performance.

The FESEM images presented in Fig. 2 show the morphological evolution of SnO_2 NPs as a function of annealing temperature. Morphology plays a pivotal role in the performance of SERS-active substrates, particularly in non-plasmonic systems where surface area, adsorption affinity, and analyte–substrate interaction dynamics are critical to signal enhancement. In the as-prepared sample (A1, Fig. 2(A) and (B)), the particles appear loosely aggregated with indistinct boundaries and a porous, irregular surface topography. These features are characteristics of sol–gel-derived oxides prior to calcination and reflect incomplete crystallization, along with a high density of surface hydroxyl groups and adsorbed by-products.[47] This morphology is consistent with the broad XRD peaks observed for sample A1, as depicted in Fig. 1, suggesting the presence of nanocrystallites embedded within amorphous or semi-crystalline domains.

Upon post-annealing at 800 °C (A2, Fig. 2(C) and (D)), a significant morphological transformation is observed. The NPs become more spherical and compact, with reduced agglomeration. This transformation indicates improved inter-particle sintering and recrystallization driven by thermally activated diffusion. The quasi-spherical morphology correlates with enhanced crystallinity and refined lattice dimensions, as confirmed by the Rietveld refinement in Fig. 1(B), suggesting that thermal treatment not only induces crystal growth but also drives the particle surface toward energetically favourable configurations. Further annealing at 900 °C (A3, Fig. 2(E)) leads to moderate grain coalescence. Although the particles remain nanosized, they exhibit neck formation, indicating the onset of particle fusion. Although crystallite size continues to increase (as supported by XRD), excessive thermal exposure may reduce surface-active sites due to decreased surface area and potentially lower defect concentration, a trade-off that can adversely impact SERS performance. This observation aligns with recent studies, showing that optimal SERS activity is achieved not at the highest crystallinity but at an intermediate regime where surface area and defect density are simultaneously optimized.[48] Fig. S3 presents the size distribution histograms estimated from the FESEM images of the SnO_2 NP samples. This indicates the growth of SnO_2 NPs with an increase in annealing temperature.

The FESEM findings are strongly supported by the local coordination distortions observed in NEXAFS (Fig. 6) and the increased oxygen vacancy density in XPS (Fig. 5). Notably, the sample annealed at 800 °C (A2) exhibits the most uniform morphology, the highest density of SERS-relevant oxygen defects, and the most balanced structural order, a combination that is critical for efficient CT between the substrate and analyte molecules. Morphological homogeneity at the nanoscale also contributes directly to SERS signal uniformity. Variations in particle size and surface roughness, typical of unoptimized metal oxide substrates, often lead to spatially heterogeneous enhancement, limiting the practical applicability of SERS substrates in real-world sensing.[49] In contrast, the SnO_2 NPs synthesized here exhibit morphology control comparable to mesoporous TiO_2 and hierarchical ZnO systems, but with greater thermal stability and a simpler synthesis route.[50,51]

High-resolution imaging is complemented by Energy Dispersive X-ray Spectroscopy (EDS) analysis (Fig. 2(F)), which confirms the presence of Sn and O in the expected 1 : 2 stoichiometry. The absence of extraneous elements, such as residual chloride, organic contaminants, or metal dopants, validates the effectiveness of the washing, drying, and calcination steps. This chemical purity is essential, as even trace surface impurities can act as competitive adsorption centers, diminishing the specificity and reproducibility of SERS signals. Additionally, the spherical particle morphology observed in annealed samples is advantageous for analyte molecule immobilization and surface coverage. Unlike faceted or sharp-edged nanocrystals, which can induce selective site adsorption or steric hindrance, spherical particles offer uniform curvature that promotes isotropic molecular binding,

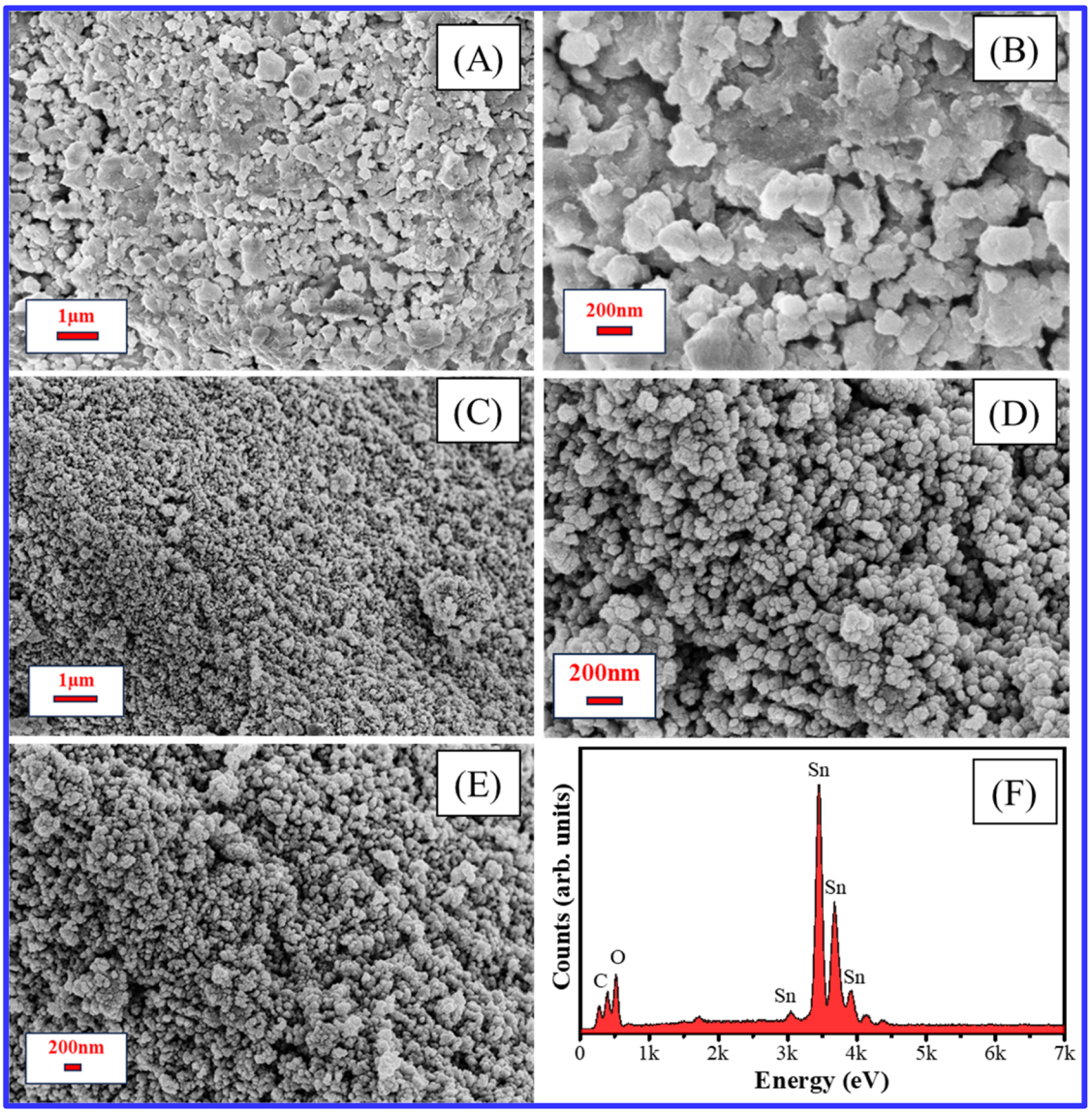

Fig. 2 FESEM micrographs of SnO_2 NPs: (A and B) as-prepared (A1), (C and D) annealed at 800 °C (A2), (E) annealed at 900 °C (A3), and (F) EDS spectrum of the A2 sample, confirming elemental composition.

enhancing spectral reproducibility. This is further supported by consistent Raman intensities recorded across multiple SERS measurements (Fig. 8), with the sample annealed at 800 °C (A2) showing stable enhancement with minimal spectral drift. From a materials design perspective, the observed morphological evolution underscores the strategic thermal tuning in SnO_2-based SERS platforms. Previous studies on Fe- and Mn-doped SnO_2 have shown that even modest changes in grain morphology can significantly affect surface charge density and electron trap distribution, which are parameters that directly influence CT efficiency.[52] In this study, annealing at 800 °C appears to optimize both surface area and defect engineering, resulting in a morphology that supports superior SERS performance.

The TEM provides high-resolution insight into the morphology, crystallinity, and size distribution of SnO_2 NPs, complementing the surface-level observations obtained by FESEM. Fig. 3(A) shows the as-prepared SnO_2 NPs (before annealing), demonstrating agglomerated amorphous-type NPs. Fig. 3(B) and (C) show the SnO_2 NPs obtained after annealing at 800 °C and 900 °C (A2 and A3 samples), respectively. As shown in Fig. 3(B) and (C), the particles show well-dispersed, spherical to quasi-spherical shapes with smooth contours and distinct boundaries across multiple magnifications. The uniform morphology observed throughout the field of view is consistent with thermally matured nanocrystals and aligns well with the grain evolution observed in the FESEM images (Fig. 2). The spherical geometry suggests isotropic growth kinetics during high-temperature annealing at 800 °C, where surface diffusion dominates particle reconfiguration. This isotropy in shape supports a uniform surface energy distribution, which is highly relevant to even analyte adsorption in SERS applications. The absence of agglomerates or interparticle necking, often observed in excessively sintered oxide systems, implies that the

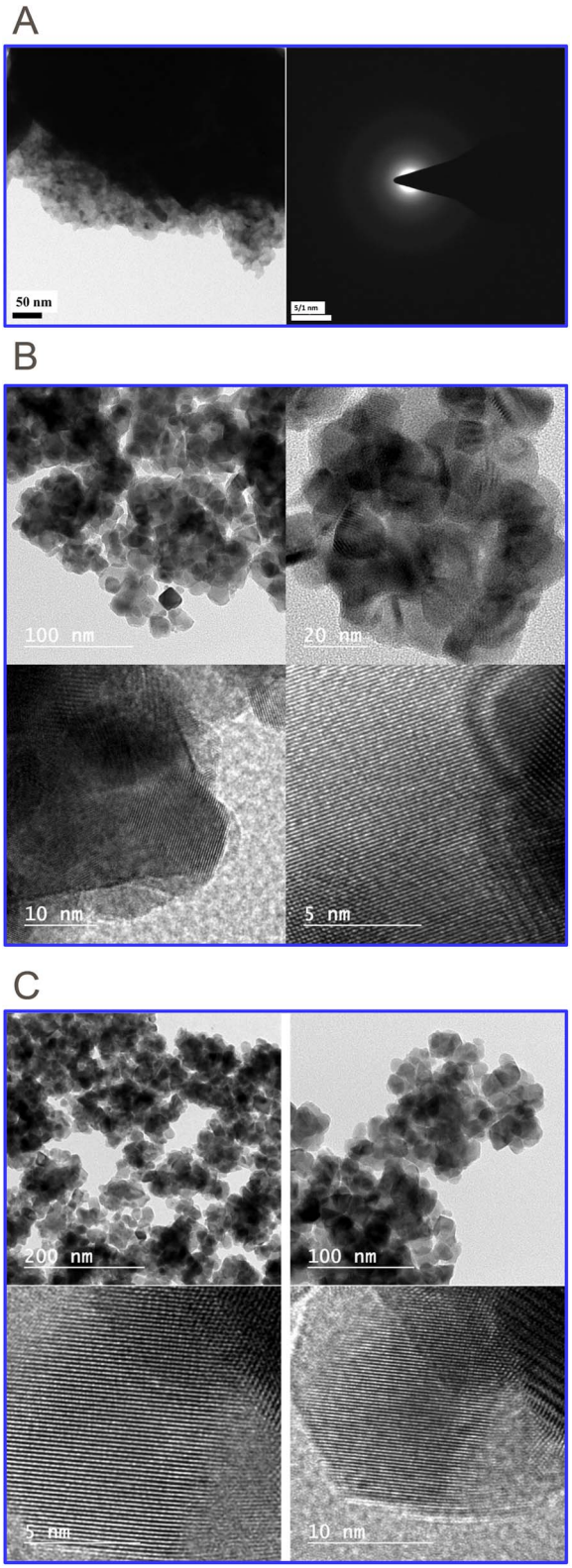

Fig. 3 (A) TEM image and the respective SAED pattern of the as-prepared SnO_2 NPs (A1). (B) TEM images at various magnifications of SnO_2 NPs annealed at 800 °C (A2). (C) TEM images at various magnifications of SnO_2 NPs annealed at 900 °C (A3).

annealing conditions were well-optimized to enhance crystallinity without compromising dispersion.

The structural uniformity is further supported by the selected area electron diffraction (SAED) patterns presented in Fig. 4(A) and (C), which exhibit concentric diffraction rings indexed to the (110), (101), (211), and (301) planes of tetragonal rutile SnO_2. The presence of discrete, continuous rings confirms the polycrystalline nature of the particles. In defect-engineered semiconductor SERS systems, such polycrystallinity is desirable, as grain boundaries can serve as preferential sites for defect formation and carrier localization, which are important contributors to CT enhancement mechanisms.[53] This interpretation correlates closely with the Rietveld refinement of the XRD results (Fig. 1(B)), confirming the long-range crystallographic order and the absence of secondary phases. At the local scale, high-resolution TEM (not shown here) reveals ordered lattice fringes across individual grains, further confirming the crystallographic coherence necessary to minimize carrier scattering and enhance photo-induced charge separation at the NP–analyte interface.

Particle size analysis reveals a narrow Gaussian distribution centred at 12 ± 0.5 nm and 17 ± 0.5 nm for the A2 and A3 samples, as presented in Fig. 4(B) and (D), respectively. This narrow polydispersity is significant for SERS applications, where size-dependent effects, such as quantum confinement and surface curvature, can strongly influence field enhancement. Uniform particle size ensures consistent hot-spot density and spatial reproducibility of Raman signals, two critical metrics in biosensing applications, especially in trace analyte detection. From a mechanistic standpoint, this particle size regime is particularly advantageous for non-plasmonic SERS. Previous studies on metal-doped ZnO and TiO_2 have demonstrated that defect-mediated CT is maximized in particles below 50 nm, where shorter diffusion paths of photo-induced carriers reduce recombination losses and enhance interfacial interactions with the analyte.[45] In our system, this is corroborated by the enhanced Raman signals observed for the NB analyte (Fig. 8), especially in the 800 °C and 900 °C annealed samples. Furthermore, this particle size and morphology correlate well with the oxygen defect concentration profiles derived from XPS (Fig. 5) and NEXAFS (Fig. 6), which confirm the presence of controlled lattice disorder and oxygen vacancies without compromising crystallinity. The spherical NPs provide a high surface-to-volume ratio, facilitating both molecular adsorption and defect-driven electronic interaction, which are two pillars of chemical enhancement in semiconductor-based SERS.

Unlike plasmonic NPs, which rely on nanoscale sharp features or interparticle gaps to generate electromagnetic hot spots, the SnO_2-based SERS substrates depend on well-distributed surface activity across each NP. The uniformity and crystalline quality observed here ensure that each particle functions as a reproducible active site for analyte–substrate interaction, promoting spectral stability over repeated SERS measurements. It is also important to note that the absence of lattice defects or faceting commonly associated with uncontrolled growth suggests that the sol–gel synthesis route, combined with thermal regulation, enabled an energetically favorable pathway for crystal

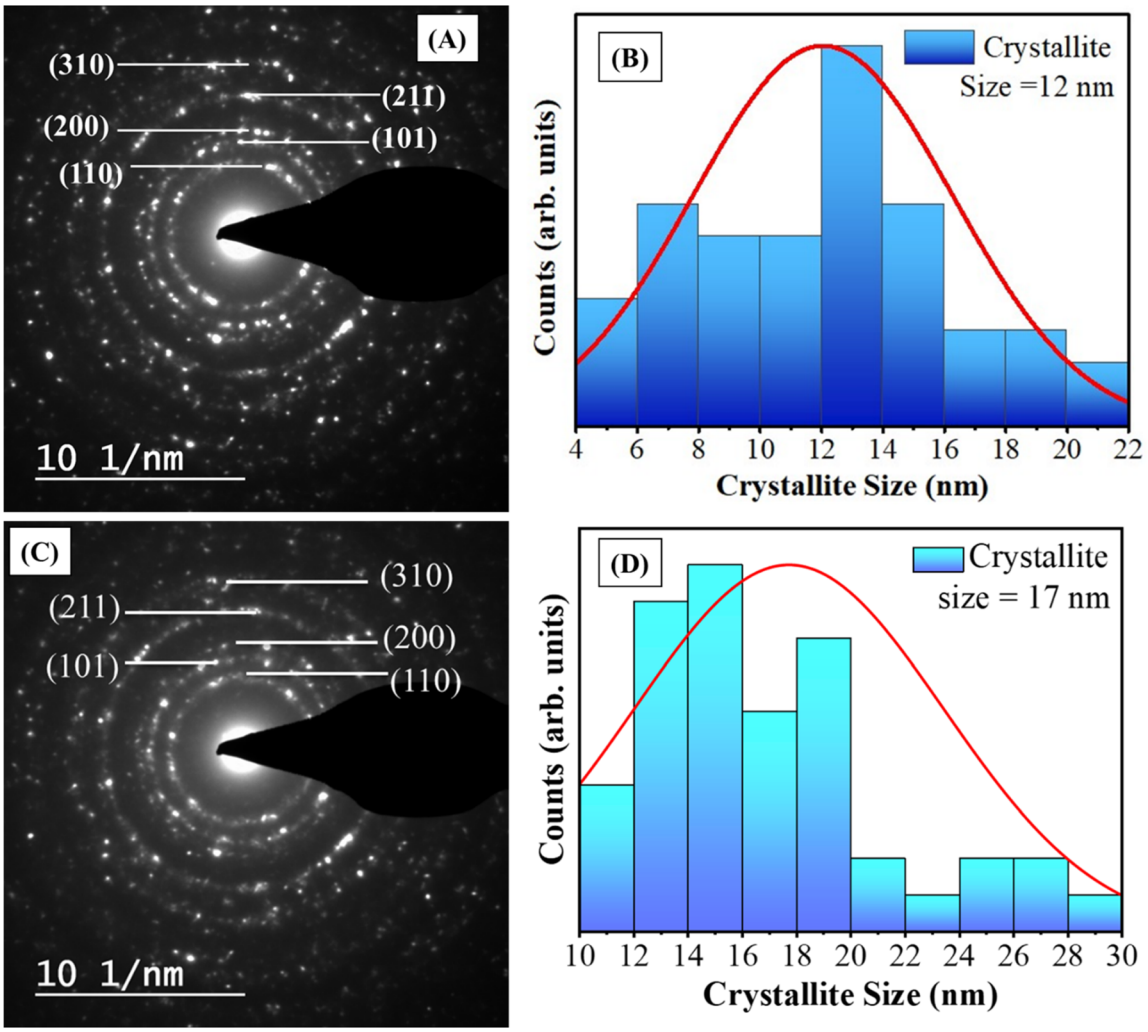

Fig. 4 (A) SAED pattern and (B) size distribution of the SnO_2 NPs (sample A2). (C) SAED pattern and (D) size distribution of the SnO_2 NPs (sample A3).

development.[54] This avoids the issue of anisotropic strain, which in many oxide systems leads to irregular surface potential landscapes and unpredictable SERS behaviour.

The XPS provides vital insight into the chemical states and surface defect landscape of the synthesized SnO_2 NPs. The survey spectrum in Fig. S4 exhibits characteristic peaks for Sn and O, with no evidence of extraneous elements, such as C, Cl, or residual precursors. This confirms the elemental purity of the annealed sample, which is consistent with the EDS results (Fig. 2(F)). Notably, the absence of metallic Sn or sub-stoichiometric tin oxides (*e.g.*, SnO and Sn_2O_3) indicates successful stabilization of the Sn^{4+} oxidation state throughout the crystal lattice. The high-resolution Sn 3d XPS spectrum depicted in Fig. 5(A) reveals two well-resolved peaks at binding energies of 486.9 eV (Sn $3d_{5/2}$) and 495.3 eV (Sn $3d_{3/2}$), which are characteristics of Sn^{4+} oxidation state in rutile SnO_2.[55] The symmetric peak shape and narrow width imply a uniform oxidation environment, which is free from sub-valent Sn species, that could introduce local heterogeneity and compromise SERS signal consistency. These observations are in good agreement with the Rietveld-refined XRD data, as depicted in Fig. 3, confirming phase-pure SnO_2, and the SAED analysis in Fig. 3(A), which demonstrates crystallographic coherence across the NP ensemble.

Of particular significance is the deconvoluted O 1s XPS spectrum shown in Fig. 5(B). Three distinct components are evident: a higher binding energy peak at 530.2 eV attributed to lattice oxygen (O_L), a lower energy peak at 531.8 eV associated with oxygen vacancies (O_V) and a chemisorbed oxygen species (O_C). The substantial area under the O_V peak indicates a high density of oxygen-related surface defects, a hallmark of defect-rich semiconductor systems optimized for chemical enhancement in SERS.[56] These vacancies play multiple roles in enhancing SERS activity. First, they act as electron donors, contributing free carriers to the conduction band (CB) and facilitating CT between the substrate and adsorbed analytes. Second, they introduce shallow energy states just below the CB edge, stabilizing molecular resonance and increasing the Raman scattering cross-section *via* chemical enhancement pathways.[18] These mechanisms are especially vital in semiconductor-based SERS, where electromagnetic enhancement is minimal or absent.

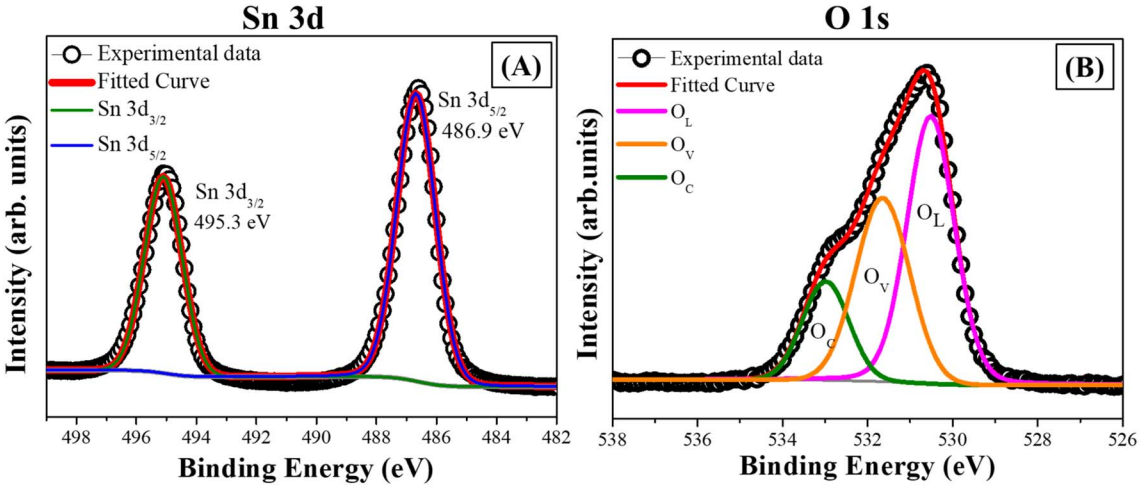

Fig. 5 (A) Sn 3d XPS spectrum confirming the Sn^{4+} state and (B) O 1s spectrum with lattice O and defect O (O vacancies) for the SnO_2 NPs of A2.

Quantitative analysis reveals that the O_V/O_L ratio is highest in the sample annealed at 800 °C (A2), confirming that thermal annealing not only promotes crystallite growth and morphological refinement but also induces beneficial lattice oxygen loss, enhancing surface reactivity and CT efficiency. This defect engineering through controlled thermal processing has been extensively reported in metal oxide-based SERS systems, such as oxygen-deficient WO_{3-x}/TiO_2 and ZnO nanosheets, where engineered O_V significantly boosted Raman sensitivity and amplified Raman signals.[57,58] The present study builds on these insights by demonstrating that SnO_2, when annealed under optimized conditions, can achieve comparable enhancement without the need for doping or plasmonic additives.

The XPS findings are further supported by O K-edge NEXAFS spectra (Fig. 6), which show attenuation in the coordination shell consistent with oxygen depletion. This convergence of global (XPS) and local (NEXAFS) spectroscopic evidence adds strong credibility to the argument that surface defect concentration is a central variable modulating SERS behaviour in the SnO_2 system. Another subtle but important detail is the binding energy of the O_V component at 531.8 eV, which is slightly lower than the typical energy for hydroxylated surface oxygen (>532.0 eV). This implies that the observed signal arises from intrinsic lattice vacancies rather than from chemisorbed water or contaminants. This distinction is critical, as true lattice O_V actively participates in charge exchange, while surface hydroxyls tend to inhibit analyte interactions and cause fluorescence interference in Raman measurements. The presence of O_V defects also explains the enhanced affinity of SnO_2 for electron-rich analytes, in which the lone pair can coordinate with the O_V site, stabilizing the molecule–substrate complex and facilitating efficient CT.

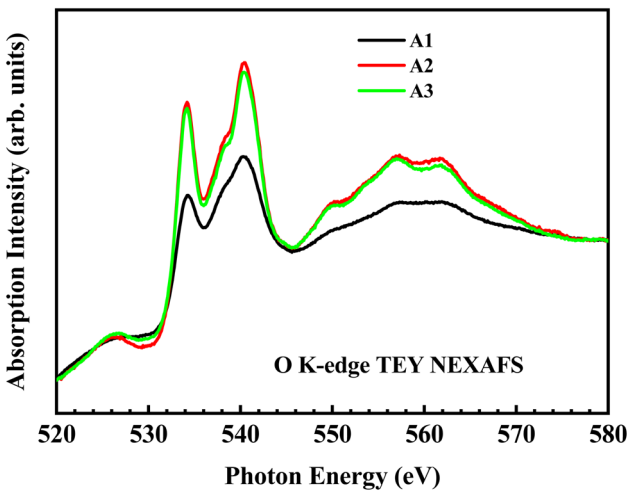

Fig. 6 O K-edge NEXAFS spectra of the as-prepared and annealed SnO_2.

The O K-edge NEXAFS spectra of the as-prepared and annealed SnO_2 samples, shown in Fig. 6, provide element-specific insights into the short-range coordination environment surrounding the oxygen atoms in the SnO_2 lattice. Unlike XRD or SAED, which probe the long-range crystallographic order, NEXAFS probes local bonding characteristics, including bond distances, coordination number, and disorder, parameters that are essential for understanding the defect landscape influencing SERS activity. In the as-prepared sample (A1), the spectrum exhibits broadened features between 530 and 534 eV, corresponding to O–Sn interactions, and a second spectral line from 534 eV to 545 eV, which is attributed to O–O correlations or multiple scattering paths within SnO_6 octahedra. These spectral features reflect a partially ordered, defect-prone lattice typical of sol–gel-derived oxides prior to thermal treatment.[37] They suggest incomplete Sn–O coordination, high microstrain, and non-ideal bond angles, which are consistent with the broadened XRD reflections illustrated in Fig. 1. Upon annealing to 800 °C (A2), the NEXAFS spectrum shows a marked increase in peak intensity and sharpness, indicating enhanced static and dynamic ordering, improved crystallinity in SnO_2, and more coherent local bonding. Importantly, oxygen vacancies remain present, as evidenced by subtle deviations from ideal coordination. These defects are not residual artifacts but intentional

structural features that play a central role in the chemical enhancement mechanism in semiconductor-based SERS.

Oxygen vacancies introduce localized electronic states below the CB edge, providing low-energy pathways for CT from the semiconductor to adsorbed analyte molecules, a mechanism distinct from the electromagnetic enhancement dominant in plasmonic systems.[18] The sample annealed at 900 °C (A3) exhibits partial restoration of the local order, but the spectrum does not fully revert to the sharpness of A1, implying that while grain growth and reordering occur, a fraction of thermally generated vacancies remains trapped within the lattice. This observation aligns with the crystallite size evolution from the XRD patterns and the narrowing particle size distribution observed in the TEM. These defect-stabilized lattices are known to be advantageous for applications requiring both surface sensitivity and structural robustness, such as SERS and gas sensing.[10] The difference in spectral intensity between the A1 and A2 samples reveals that annealing at 800 °C is the thermodynamically favourable condition for generating a high density of SERS-active surface defects without destabilizing the lattice framework. The NEXAFS-derived reduction in the coordination number (CN), from the ideal values of 6 in perfect SnO_6 octahedra to approximately 5 or lower in defect-rich regions,[59] directly affects local charge distribution and surface polarity. These changes enhance analyte adsorption and promote charge coupling, as previously reported in TiO_2 and SnO_2 systems.[45]

The presence of vacancies enables orbital overlap between the CB of SnO_2 and the lowest unoccupied molecular orbital (LUMO) of the probe molecule, facilitating rapid electron transfer under illumination.[45] Notably, NEXAFS analysis confirms that these vacancies are embedded within the lattice rather than being surface-adsorbed oxygen species. This distinction is crucial, as lattice vacancies are electronically active, while surface hydroxyls or physiosorbed oxygen, often detected by XPS, do not significantly contribute to Raman enhancement unless they are involved in redox processes.[60] The correlation between NEXAFS, XPS, TEM, and SERS performance underscores a central design principle: optimal SERS sensitivity does not require perfect crystallinity, but rather a finely tuned balance between structural order and localized disorder. Excessive vacancies can destabilize the structure or cause non-radiative recombination, while insufficient vacancies render the CT pathway inactive. Among the samples studied, A2 (annealed at 800 °C) achieves this balance most effectively, exhibiting structural coherence, morphological uniformity, and electronically active defects. Fig. S5 presents the diffuse reflectance spectra of SnO_2 NPs and the respective estimated band edge positions for the SnO_2 samples. It gives that with annealing temperatures, the bandgap is reduced from 4.2 eV to 3.97 eV for the A1 to A3 samples, respectively. This indicates a more stable phase of SnO_2 formation with an increase in temperature, and with annealing temperature, we can tune the bandgap of SnO_2 NPs.

The Raman spectra of SnO_2 NPs, presented in Fig. 7, offer a phonon-level view of their crystalline integrity, structural reorganization, and defect population, which are vital factors influencing CT dynamics in SERS. As a non-centrosymmetric material with tetragonal rutile symmetry, SnO_2 exhibits multiple Raman-active vibrational modes arising from collective lattice motions of Sn and O atoms. The Raman spectrum of the as-prepared sample (A1) displays broad and weak bands centered near 476 and 776 cm^{-1}, corresponding to first-order E_g and B_{2g} modes of the rutile SnO_2 phase, respectively, while another band at 633 cm^{-1} (A_{1g} mode) becomes prominent, and the peak sharpness and intensity of all modes increase markedly in annealed samples A2 and A3.[61] The A_{1g} mode corresponds to the symmetric stretching vibration of bridging oxygen atoms in the Sn–O–Sn framework, while the E_g and B_{2g} modes arise from bending and asymmetric stretching, respectively.

The broadness and low intensity of these modes in sample A1 suggest poor crystallinity, high microstrain, and possible short-range disorder, which is consistent with the XRD results, revealing broadened diffraction peaks and limited structural coherence. Upon annealing at 800 °C (A2), the A_{1g} mode becomes sharper and shifts slightly to a lower wavenumber (630 cm^{-1}), indicating relaxation of the internal lattice strain and improved long-range order. This phonon sharpening and red shift are classical indicators of grain coarsening and lattice stress relief, corroborated by Rietveld refinement, which confirmed near-ideal lattice parameters. The enhanced intensity of the E_g and B_{2g} modes further reflects improved structural coherence and reduced grain boundary scattering.[62] In the sample annealed at 900 °C (A3), the Raman signals remain intense but show slight broadening, especially in the E_g and B_{2g} bands. This may indicate the onset of grain coalescence or

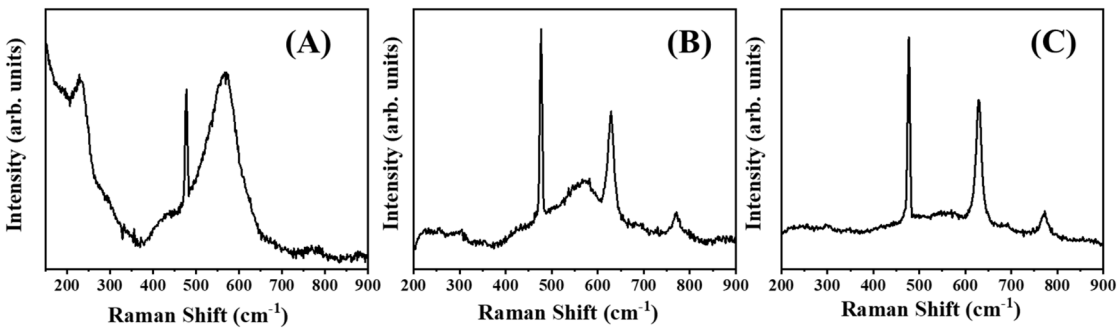

Fig. 7 Raman spectra of (A) as-prepared SnO_2 sample, (B) sample annealed at 800 °C, and (C) sample annealed at 900 °C, showing increased signal sharpness and intensity with thermal treatment.

partial healing of oxygen vacancy density, which are trends also observed in XPS and NEXAFS, suggesting reduced defect density at higher annealing temperatures. These subtle spectral changes reinforce the importance of balancing crystallinity and defect concentration to optimize surface reactivity and CT efficiency in semiconductor-based SERS platforms.

Although the A_{1g} mode is not a direct fingerprint of oxygen vacancies, its line width and symmetry are highly sensitive to lattice imperfections. Studies on vacancy-rich SnO_2 and doped analogues have shown that A_{1g} mode broadening or shoulder formation correlates with non-bridging oxygen species or local distortions.[63] In the present study, the A2 sample exhibits the optimal trade-off: sharp phonon features indicate structural order, alongside defect-rich signatures confirmed by XPS and NEXAFS, suggesting the active involvement of these phonons in SERS enhancement mechanisms. This balance is particularly crucial when transitioning from intrinsic Raman to SERS measurements. As shown in Fig. 8(B), the A2 sample exhibits the highest SERS response, indicating that vibrational uniformity coupled with localized oxygen defects creates ideal conditions for analyte–substrate CT. The enhanced intensity and spectral clarity in the A_{1g} mode also imply increased surface polarizability, which amplifies the Raman polarizability tensor, a prerequisite for both chemical enhancement and CT-driven mechanisms in semiconducting SERS systems.[64]

Furthermore, no extraneous peaks associated with carbonaceous contamination, hydroxylation, or phase impurities confirm the purity of the SnO_2 phase, as supported by EDS and XPS. The absence of parasitic bands is observed in the 300–400 cm^{-1} region, ruling out the formation of intermediate tin oxides (*e.g.*, SnO and Sn_2O_3) that could interfere with analyte signal interpretation.[65] Comparative analysis with doped SnO_2 further highlights the advantages of thermal defect engineering. In Fe- and Mn-doped SnO_2, Raman mode broadening and red-shifting are widely reported due to increased lattice distortion from ionic radius mismatches.[43,52] In contrast, the undoped but thermally optimized SnO_2 presented here retains phase integrity while introducing active defect states, offering a scalable and cost-effective route to a high-performance SERS substrate. Finally, the reproducibility and high signal-to-noise

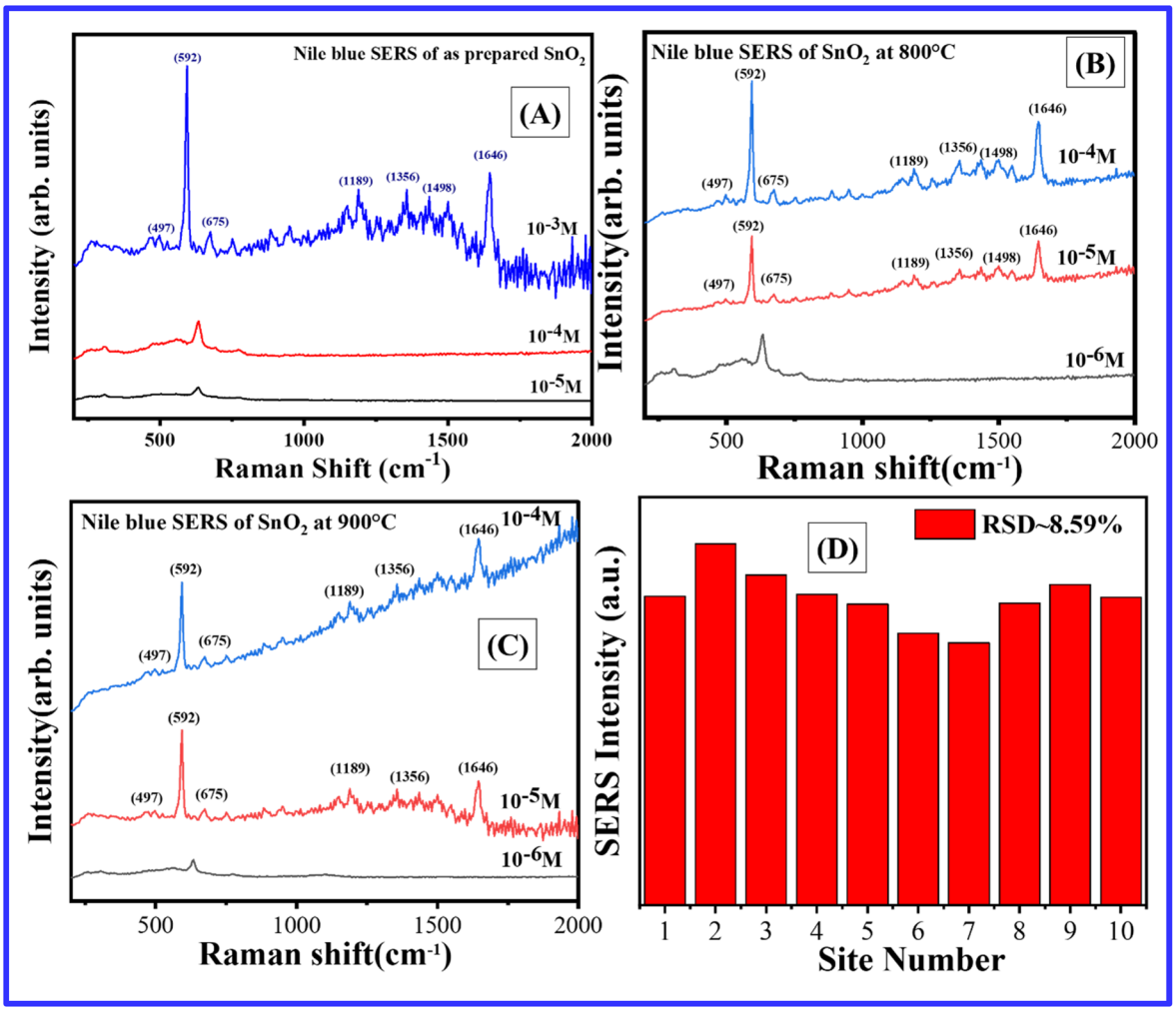

Fig. 8 (A)–(C) SERS spectra of Nile blue dye at various concentrations using different SnO_2 NPs from the A1, A2, and A3 samples. (D) Relative standard deviation (RSD) of Raman modes at 592 cm^{-1} from 10 multiple spots observed in the A2 sample.

Table 2 Comparison of enhancement factors and detection limits of various oxide semiconductors

Materials	EF	LOD (mol L^{-1})	Comments	Reference
Si grating array	$\sim 7.3 \times 10^6$	10^{-11}	Good signal uniformity	9
WO_{3-x}/TiO_2	1.2×10^5	10^{-10}	Stable dual functional material	40
Al/ZnO/Ag	2.45×10^8	10^{-13}		49
Ag/ZnO	$\sim 2.7 \times 10^8$	10^{-13}		50
Au nanofoam	7.3×10^8	—	Inexpensive, simple, robust	69
TiN/ZnO nanowires	$\cong 1.10 \times 10^2$	—	Cost-effective scale up	70
Ag/TiO_2	$\cong 10^5$	10^{-3}	Plasmonic, expensive	71
Metal-doped oxide	$\cong 10^4$	10^{-3}	Few defects, lower enhancement	72
ZnO NPs	$\sim 10^3$	—	20 nm ZnO NPs used	73
TiO_2	$\sim 10^2$	—		74
CuO	$\sim 10^2$	—		75
SnO_2 NPs	$\cong 3.95 \times 10^3$	4.23×10^{-6}	Low-cost, scalable, defect-assisted, chemically robust, and reusable	This study

ratio of the Raman spectra, particularly for the A2 sample, establish this annealed SnO_2 as a structurally and spectroscopically stable platform for SERS applications. The intrinsic vibrational signature captured here serves as a reliable baseline for identifying molecular vibrational modes in analyte-loaded spectra, as demonstrated in Fig. 8, with NB analyte.

Fig. 8(A)–(C) presents the SERS spectra of NB recorded on samples A1, A2, and A3, respectively. The selected analyte, NB, a heterocyclic dye with well-characterized vibrational modes, is widely used as a benchmark analyte due to its high polarizability and sensitivity to local dielectric environments.[66] The spectra exhibit distinct and well-resolved peaks at 591, 1147, 1360, and 1630 cm^{-1}, corresponding to C–C skeletal deformation, aromatic C–H in-plane bending, C–N stretching, and ring-breathing vibrations, respectively.[67] These modes are particularly sensitive to electron density fluctuations within the molecule, and their intensities serve as reliable indicators of substrate–analyte interaction strength.

At a concentration of 10^{-4} mol L^{-1}, all major NB vibrational modes appear intense and symmetric, indicating effective analyte adsorption and strong resonance conditions on the SnO_2 surface. Remarkably, these modes remain detectable at lower concentrations of 10^{-5} and 10^{-6} mol L^{-1} without significant baseline distortion or peak merging. This highlights the substrate's ability to maintain consistent enhancement even at ultra-low analyte loadings, a challenge for traditional plasmonic SERS systems, where signal reproducibility drops sharply with dilution. This robust performance arises from the defect-engineered semiconducting nature of the SnO_2 substrate. Unlike plasmonic metals that rely on electromagnetic field enhancement at nanoscale features, SnO_2 enhances Raman signals primarily through a chemical enhancement mechanism dominated by CT. This process requires favourable energy alignment between the semiconductor's CB and the LUMO of the analyte. Oxygen vacancies, confirmed *via* XPS and NEXAFS, introduce mid-gap states that lower the effective CB minimum and facilitate efficient electron donation to the NB molecule. Additionally, the high density of vacancy sites increases surface dipole moments and creates localized regions of high electron density, promoting analyte anchoring and stabilization. As a result, molecules are held close to the surface in a configuration conducive to orbital overlap, ensuring efficient coupling and enhancing polarizability under laser excitation. These effects are supported by the uniform particle morphology and narrow size distribution observed in TEM, which minimizes field inhomogeneities and ensures consistent analyte exposure across the substrate. Fig. 8(D) shows the relative standard deviation (RSD) of Raman modes at a wavenumber of 592 cm^{-1} from different regions observed in the A2 sample.

A particularly noteworthy feature is the absence of a fluorescence background, even at low analyte concentrations. In metal-based SERS systems, NB often exhibits intense fluorescence that can obscure weak Raman signals, especially in the 600–800 cm^{-1} range.[68] The wide bandgap and non-resonant optical character of SnO_2-based platform suppress this interference, allowing for clean detection of vibrational modes, which is a considerable advantage for biological and environmental sensing applications. The quantitative enhancement factor (EF) was calculated using the following standard formula:[69]

$$\mathrm{EF} = \left(\frac{I_{\mathrm{SERS}}}{I_{\mathrm{Bulk}}}\right) \times \left(\frac{C_{\mathrm{Bulk}}}{C_{\mathrm{SERS}}}\right).$$

Assuming bulk NB intensity (I_{Bulk}) at a concentration (C_{Bulk}) of 10^{-2} mol L^{-1} and SERS intensity (I_{SERS}) at a concentration (C_{SERS}) of 10^{-6} mol L^{-1}, the EF was estimated to be approximately 3.95×10^3. Comparative EFs for various systems are illustrated in Table 2. Although this value is modest compared to plasmonic substrates (typical EF of 10^5–10^7), it is considered excellent for pure semiconductors without metal decoration, as reported in doped ZnO, TiO_2, and Fe_2O_3 systems.[11] Moreover, the ability to detect NB down to 10^{-6} mol L^{-1} positions this system within the sensitivity range required for environmental toxins and biochemical markers. The system's responsiveness to NB confirms that analyte–substrate energy coupling, rather than solely molecular cross-section, governs signal intensity, a principle consistent with CT theory in SERS.[70] Furthermore, the uniformity of the Raman signal across the concentration gradient, evidenced by consistent peak positions, absence of band splitting, and minimal noise, attests to substrate homogeneity, which is previously validated by Rietveld refinement, SAED, and Raman analyses. This level of reproducibility is rare in non-lithographic SERS platforms and positions the SnO_2 system as a promising candidate for scalable, low-cost, and on-site chemical sensing platforms.

4. Conclusions

In this study, phase-pure, nanocrystalline SnO_2 NPs were successfully synthesized using a sol–gel-assisted method and structurally optimized through thermal annealing at 800 and 900 °C. Comprehensive structural, morphological, and local coordination analyses confirmed that thermal treatment promoted crystallinity and spherical particle morphology (~33 nm) and induced a controlled increase in oxygen vacancies without compromising lattice integrity. Among the annealed samples, SnO_2 NPs treated at 800 °C exhibited the highest vacancy concentration, resulting in surface-active defect states that facilitate CT, the dominant enhancement mechanism in non-plasmonic SERS. Raman spectroscopy validated the improved phonon activation and crystallinity, while SERS measurements using Nile blue demonstrated significant enhancement with an estimated EF of approximately 3.95×10^3 and a detection limit of 10^{-6} mol L^{-1}. Critically, the optimal balance between lattice order and surface disorder achieved at 800 °C translated into superior SERS response, high spectral reproducibility, and stable detection across a wide analyte concentration range, all accomplished without the use of noble metals or dopants. These findings underscore the potential of defect-engineered SnO_2 as a low-cost, scalable, and chemically active SERS platform. This study demonstrates that the rational thermal engineering of metal oxide NPs can produce robust and reproducible substrates for molecular sensing. It opens promising avenues for the development of metal-free, oxide-based SERS systems applicable to environmental monitoring and biosensor technologies.

Conflicts of interest

The authors declare that there are no conflicts to declare.

Data availability

The data supporting the findings of this study are given in the manuscript, and data files are available from the corresponding author upon request.

Supplementary information (SI) is available. See DOI: https://doi.org/10.1039/d5ra08335d.

Acknowledgements

The authors acknowledge the Centre for Nanotechnology, University of Hyderabad, for providing micro-Raman facilities. PSL acknowledges GITAM management for supporting with the MURTI excellence fellowship.

References

1 D. L. Jeanmaire and R. P. Van Duyne, Surface Raman spectroelectrochemistry. Part I. Heterocyclic, aromatic, and aliphatic amines adsorbed on the anodized silver electrode, *J. Electroanal. Chem.*, 1977, **84**(1), 1–20, DOI: 10.1016/S0022-0728(77)80224-6.

2 G. M. Das, S. Managò, M. Mangini and A. C. De Luca, Biosensing using sers active gold nanostructures, *Nanomaterials*, 2021, **11**(10), 2679, DOI: 10.3390/nano11102679.

3 K. Kneipp, *et al.*, Single molecule detection using surface-enhanced Raman scattering (SERS), *Phys. Rev. Lett.*, 1997, **78**(9), 1667–1670, DOI: 10.1103/PhysRevLett.78.1667.

4 Z. Q. Tian, B. Ren and D. Y. Wu, Surface-enhanced Raman scattering: From noble to transition metals and from rough surfaces to ordered nanostructures, *J. Phys. Chem. B*, 2002, **106**(37), 9463–9483, DOI: 10.1021/jp0257449.

5 S. Park, J. Lee and H. Ko, Transparent and Flexible Surface-Enhanced Raman Scattering (SERS) Sensors Based on Gold Nanostar Arrays Embedded in Silicon Rubber Film, *ACS Appl. Mater. Interfaces*, 2017, **9**(50), 44088–44095, DOI: 10.1021/acsami.7b14022.

6 Z. Tu, M. Kunimoto, M. Yanagisawa and T. Homma, Fabrication of a plasmonic sensor for surface-enhanced Raman spectroscopy using electroless deposition of Ag with hypophosphite, *Electrochem. Commun.*, 2023, **152**, 107513, DOI: 10.1016/j.elecom.2023.107513.

7 K. Kant, *et al.*, Plasmonic nanoparticle sensors: current progress, challenges, and future prospects, *Nanoscale Horiz.*, 2024, **9**(12), 2085–2166, DOI: 10.1039/d4nh00226a.

8 L. Keerthana, M. Ahmad Dar and G. Dharmalingam, Plasmonic Au-Metal Oxide Nanocomposites for High-Temperature and Harsh Environment Sensing Applications, *Chem.–Asian J.*, 2021, **16**(22), 3558–3584, DOI: 10.1002/asia.202100885.

9 L. Wu, H. Zhou, W. He, B. Yu and L. Qian, Fabrication of large-area and highly uniform interlaced silicon grating arrays for high-performance SERS substrates, *Surf. Interfaces*, 2022, **32**, 102156, DOI: 10.1016/j.surfin.2022.102156.

10 X. Du, *et al.*, Advances in oxide semiconductors for surface enhanced Raman scattering, *Appl. Mater. Today*, 2022, **29**, 101563, DOI: 10.1016/j.apmt.2022.101563.

11 X. Wang, E. Zhang, H. Shi, Y. Tao and X. Ren, Semiconductor-based surface-enhanced Raman scattering (SERS): from active materials to performance improvement, *Analyst*, 2022, **147**(7), 1257–1272, DOI: 10.1039/d1an02165f.

12 S. Das and V. Jayaraman, SnO2: A comprehensive review on structures and gas sensors, *Prog. Mater. Sci.*, 2014, **66**, 112–255, DOI: 10.1016/j.pmatsci.2014.06.003.

13 M. Karmaoui, *et al.*, One-Step Synthesis, Structure, and Band Gap Properties of SnO2 Nanoparticles Made by a Low Temperature Nonaqueous Sol-Gel Technique, *ACS Omega*, 2018, **3**(10), 13227–13238, DOI: 10.1021/acsomega.8b02122.

14 E. Skripkin, *et al.*, Fast and ecofriendly triple sulfonamides mixture utilization using UV irradiation and spherical SnO2 nanoparticles with controllable parameters and antibacterial activity, *Chemosphere*, 2024, **349**, 140981, DOI: 10.1016/j.chemosphere.2023.140981.

15 Y. Doubi, *et al.*, Controlled SnO2 nanostructures for enhanced sensing of hydrogen sulfide and nitrogen

dioxide, *Sens. Actuators, B*, 2025, **440**, 137878, DOI: 10.1016/j.snb.2025.137878.
16 Y. Li, Z. Yuan, F. Meng, Y. Shen and C. Xing, Gas Sensor Based on ZnSnO/SnO Nanocubes for Rapid N-Propanol Detection, *IEEE Trans. Instrum. Meas.*, 2022, **71**, 1–8, DOI: 10.1109/TIM.2022.3217567.
17 B. Sharma, R. R. Frontiera, A. I. Henry, E. Ringe and R. P. Van Duyne, SERS: Materials, applications, and the future, *Mater. Today*, 2012, **15**(1–2), 16–25, DOI: 10.1016/S1369-7021(12)70017-2.
18 G. Song, S. Cong and Z. Zhao, Defect engineering in semiconductor-based SERS, *Chem. Sci.*, 2022, **13**(5), 1210–1224, DOI: 10.1039/d1sc05940h.
19 J. Ye, *et al.*, Understanding the Chemical Mechanism behind Photoinduced Enhanced Raman Spectroscopy, *J. Phys. Chem. Lett.*, 2023, **14**(19), 4607–4616, DOI: 10.1021/acs.jpclett.3c00478.
20 R. Ponte, E. Rauwel and P. Rauwel, Tailoring SnO2 Defect States and Structure: Reviewing Bottom-Up Approaches to Control Size, Morphology, Electronic and Electrochemical Properties for Application in Batteries, *Materials*, 2023, **16**(12), 4339, DOI: 10.3390/ma16124339.
21 S. Ghosal, S. Nandi and P. K. Giri, Recent advances in semiconductor nanostructure-based surface-enhanced Raman scattering sensors, *Nanotechnology*, 2025, **36**(20), 202002, DOI: 10.1088/1361-6528/adcbaf.
22 M. J. Limo, *et al.*, Interactions between Metal Oxides and Biomolecules: From Fundamental Understanding to Applications, *Chem. Rev.*, 2018, **118**(22), 11118–11193, DOI: 10.1021/acs.chemrev.7b00660.
23 K. V. Serebrennikova, N. S. Komova, A. V. Zherdev and B. B. Dzantiev, SERS Sensors with Bio-Derived Substrates Under the Way to Agricultural Monitoring of Pesticide Residues, *Biosensors*, 2024, **14**(12), 573, DOI: 10.3390/bios14120573.
24 S. Jin, D. Zhang, B. Yang, S. Guo, L. Chen and Y. M. Jung, Noble metal-free SERS: mechanisms and applications, *Analyst*, 2023, **149**(1), 11–28, DOI: 10.1039/d3an01669b.
25 W. Chen, D. Ghosh and S. Chen, Large-scale electrochemical synthesis of SnO2 nanoparticles, *J. Mater. Sci.*, 2008, **43**(15), 5291–5299, DOI: 10.1007/s10853-008-2792-x.
26 Z. R. Dai, J. L. Gole, J. D. Stout and Z. L. Wang, Tin Oxide Nanowires, Nanoribbons, and Nanotubes, *J. Phys. Chem. B*, 2002, **106**(6), 1274–1279, DOI: 10.1021/jp013214r.
27 Y. Liu, J. Dong and M. Liu, Well-Aligned "Nano-Box-Beams" of SnO2, *200306104 Advanced Materials*, 2004, **16**(4), 353–356, DOI: 10.1002/adma.
28 H. Mahmood, M. A. Khan, B. Mohuddin and T. Iqbal, Solution-phase growth of tin oxide (SnO2) nanostructures: Structural, optical and photocatalytic properties, *Mater. Sci. Eng., B*, 2020, **258**, 114568.
29 T. Minami, H. Nanto and S. Takata, Highly Conducting and Transparent SnO2 Thin Films Prepared by RF Magnetron Sputtering on Low-Temperature Substrates, *Jpn. J. Appl. Phys.*, 1988, **27**, L287, DOI: 10.1143/JJAP.27.L287.
30 J. G. Zhou, H. T. Fang, J. M. Maley, J. Y. P. Ko, M. Murphy, Y. Chu, R. Sammynaiken and T. K. Sham, An X-ray absorption, photoemission, and Raman study of the interaction between SnO2 nanoparticle and carbon nanotube, *J. Phys. Chem. C*, 2009, **113**(15), 6114–6117, DOI: 10.1021/jp810639y.
31 W. Q. Han and A. Zettl, Coating Single-Walled Carbon Nanotubes with Tin Oxide, *Nano Lett.*, 2003, **3**(5), 681–683, DOI: 10.1021/nl034142d.
32 C. Ge, J. Li, B. He, Y. Gu, Y. Tang and T. Li, Oxygen vacancy-enriched SnO 2/NiO n–p heterointerfaces for high-efficiency oxygen evolution reaction catalysis, *Nanoscale*, 2025, **17**(43), 24990–24998, DOI: 10.1039/D5NR03372A.
33 P. V. P. Madduri and S. N. Kaul, Intrinsic chiral-spin glass and spin glass transitions in compacted Ni5Al3/NiO core/shell nanoparticles, *Phys. Rev. Mater.*, 2019, **3**(12), 126003, DOI: 10.1103/PhysRevMaterials.3.126003.
34 P. V. P. Madduri and S. N. Kaul, Core and surface/interface magnetic anisotropies in nanocrystalline nickel, *J. Alloys Compd.*, 2016, **689**, 533–541, DOI: 10.1016/j.jallcom.2016.07.256.
35 N. C. Halder and C. N. J. Wagner, Separation of particle size and lattice strain in integral breadth measurements, *Acta Crystallogr.*, 1966, **20**(2), 312–313, DOI: 10.1107/s0365110x66000628.
36 A. Sharma, J. P. Singh, S. O. Won, K. H. Chae, S. K. Sharma, and S. Kumar, "Introduction to X-Ray Absorption Spectroscopy and Its Applications in Material Science, in *Handbook of Materials Characterization*, Cham, Springer International Publishing, 2018, pp. 497–548, DOI: 10.1007/978-3-319-92955-2_13.
37 C. Nuțescu Duduman, M. I. Barrena Pérez, J. M. Gómez De Salazar Y Caso De Los Cobos, I. Carcea, D. L. Chicet and I. Palamarciuc, Synthesis of SnO2 by Sol-Gel method, *Solid State Phenom.*, 2016, **254**, 200–206, DOI: 10.4028/www.scientific.net/SSP.254.200.
38 Q. Xiao, R. Wang and L. Xu, Annealing treatment of the SnO2 thin film prepared by sol-gel method, *Adv. Mater. Res.*, 2011, **331**, 194–197, DOI: 10.4028/www.scientific.net/AMR.331.194.
39 S. Mehraj, M. S. Ansari and Alimuddin, Annealed SnO2 thin films: Structural, electrical and their magnetic properties, *Thin Solid Films*, 2015, **589**, 57–65, DOI: 10.1016/j.tsf.2015.04.065.
40 X. He, Y. Gong, L. Niu and C. Li, Development of Defect-Rich WO3-x/TiO2 Heterojunction Toward Dual-Functional Enhancement: Boosting SERS and Photocatalytic Performance, *Nanomaterials*, 2025, **15**(7), 521, DOI: 10.3390/nano15070521.
41 Y. Shi, *et al.*, Thermal treatment induced the surface enhanced Raman scattering of WO3-TiO2 heterogeneous composite films, *Appl. Surf. Sci.*, 2023, **613**, 155975, DOI: 10.1016/j.apsusc.2022.155975.
42 F. Aydın Ünal, Synthesis and characterization of the doped/co-doped SnO 2 nanoparticles by the sol–gel method, *Int. J. Appl. Ceram. Technol.*, 2025, **22**(1), e14916, DOI: 10.1111/ijac.14916.
43 J. G. Sotelo, J. Bonilla-Ríos and J. L. Gordillo, Enhance Ethanol Sensing Performance of Fe-Doped Tetragonal SnO2 Films on Glass Substrate with a Proposed

Mathematical Model for Diffusion in Porous Media, *Sensors*, 2024, **24**(14), 4560, DOI: 10.3390/s24144560.

44 H. W. Kim, S. H. Shim and C. Lee, SnO2 microparticles by thermal evaporation and their properties, *Ceram. Int.*, 2006, **32**(8), 943–946, DOI: 10.1016/j.ceramint.2005.06.015.

45 V. R. Samriti, R. K. Gupta and J. Prakash, Engineering metal oxide semiconductor nanostructures for enhanced charge transfer: fundamentals and emerging SERS applications, *J. Mater. Chem. C*, 2022, **10**(1), 73–95, DOI: 10.1039/d1tc04886d.

46 M. Shaban Tameh, W. L. Gladfelter and J. D. Goodpaster, Unraveling Surface Chemistry of SnO2 Through Formation of Charged Oxygen Species and Oxygen Vacancies, *Int. J. Quantum Chem.*, 2025, **125**(4), e70017, DOI: 10.1002/qua.70017.

47 S. K. Sharma, P. Das and B. K. Sanfui, Unveiling the role of structure-property correlation and its validation towards engineering the application potential of sol-gel derived mesoporous gamma-alumina, *Mol. Syst. Des. Eng.*, 2022, **7**(1), 67–91, DOI: 10.1039/d1me00102g.

48 Z. Xie, S. Shuang, L. Ma, F. Zhu, X. Liu and Z. Zhang, Annealing effect on the photoelectrochemical and photocatalytic performance of TiO2 nanorod arrays, *RSC Adv.*, 2017, **7**(81), 51382–51390, DOI: 10.1039/c7ra09801d.

49 X. Chen, *et al.*, Aluminum sheet-induced porous zinc oxide nanosheets decorated with silver nanoparticles for ultrasensitive SERS sensing of crystal violet, *Mater. Adv.*, 2022, **3**(5), 2583–2590, DOI: 10.1039/d1ma01181b.

50 N. Li, G. Xu, M. Yan, B. Chen, Y. Yuan and C. Zhu, Fabrication of Vertically Aligned ZnO Nanorods Modified with Dense Silver Nanoparticles as Effective SERS Substrates, *Chemosensors*, 2023, **11**(4), 210, DOI: 10.3390/chemosensors11040210.

51 Y. Wang, *et al.*, Effect of TiO2arrays on surface-enhanced Raman scattering (SERS) performance for Ag/TiO2substrates, *Nanotechnology*, 2021, **32**(7), 075708, DOI: 10.1088/1361-6528/abc5f4.

52 N. Salah, S. Habib, A. Azam, M. S. Ansari and W. M. Al-Shawafi, Formation of Mn-doped SnO2 nanoparticles via the microwave technique: Structural, optical and electrical properties, *Nanomater. Nanotechnol.*, 2016, **6**(1), 17, DOI: 10.5772/62520.

53 V. Archana, L. Mohan, P. Kathirvel and S. Saravanakumar, Grain boundary effect on structural, optical, and electrical properties of sol-gel synthesized Fe-doped SnO2 nanoparticles, *Chin. Phys. B*, 2021, **30**(4), 048202, DOI: 10.1088/1674-1056/abc2c1.

54 S. Bertucci, *et al.*, Mild Sol-Gel Conditions and High Dielectric Contrast: A Facile Processing toward Large-Scale Hybrid Photonic Crystals for Sensing and Photocatalysis, *ACS Appl. Mater. Interfaces*, 2022, **14**(17), 19806–19817, DOI: 10.1021/acsami.1c23653.

55 F. H. Aragón, *et al.*, Structural and surface study of praseodymium-doped SnO2 nanoparticles prepared by the polymeric precursor method, *J. Phys. Chem. C*, 2015, **119**(16), 8711–8717, DOI: 10.1021/acs.jpcc.5b00761.

56 M. A. Mashkovtsev, *et al.*, Unraveling Oxygen Vacancies Effect on Chemical Composition, Electronic Structure and Optical Properties of Eu Doped SnO2, *Nanomaterials*, 2024, **14**(20), 1675, DOI: 10.3390/nano14201675.

57 X. He, Y. Gong, L. Niu and C. Li, Development of Defect-Rich WO3-x/TiO2 Heterojunction Toward Dual-Functional Enhancement: Boosting SERS and Photocatalytic Performance, *Nanomaterials*, 2025, **15**(7), 521, DOI: 10.3390/nano15070521.

58 J. Lin, *et al.*, Low temperature-boosted high efficiency photo-induced charge transfer for remarkable SERS activity of ZnO nanosheets, *Chem. Sci.*, 2020, **11**(35), 9414–9420, DOI: 10.1039/d0sc02712j.

59 Q. Zhu, Q. Ma, D. B. Buchholz, R. P. H. Chang, M. J. Bedzyk and T. O. Mason, Structural anisotropy in amorphous SnO2 film probed by X-ray absorption spectroscopy, *Appl. Phys. Lett.*, 2013, **103**(3), 031913, DOI: 10.1063/1.4815984.

60 A. van Veelen, P. C. M. Francisco, N. P. Edwards, J. F. W. Mosselmans, T. Sato and R. A. Wogelius, In situ exafs study of sr adsorption on tio2 (110) under high ionic strength wastewater conditions, *Minerals*, 2021, **11**(12), 1386, DOI: 10.3390/min11121386.

61 I. Rawal, Facial synthesis of hexagonal metal oxide nanoparticles for low temperature ammonia gas sensing applications, *RSC Adv.*, 2015, **5**(6), 4135–4142, DOI: 10.1039/c4ra12747a.

62 S. S. Abbas and H. Aboud, Sol–Gel Grown SnO2 Nanoparticles: Evaluation of Structure, Morphology, and Raman Spectra, *J. Electron. Mater.*, 2017, **46**(11), 6381–6387, DOI: 10.1007/s11664-017-5663-x.

63 F. H. Aragón, *et al.*, Evidences of the evolution from solid solution to surface segregation in Ni-doped SnO2 nanoparticles using Raman spectroscopy, *J. Raman Spectrosc.*, 2011, **42**(5), 1081–1086, DOI: 10.1002/jrs.2802.

64 X. Zhang, L. Guo, P. Li, B. Zhao and B. Cui, SERS as a probe for the charge-transfer process in a coupled semiconductor nanoparticle system TiO2/MBA/PbS, *RSC Adv.*, 2017, **7**(67), 42138–42145, DOI: 10.1039/c7ra07289a.

65 E. Fazio, F. Neri, S. Savasta, S. Spadaro and S. Trusso, Surface-enhanced Raman scattering of SnO 2 bulk material and colloidal solutions, *Phys. Rev. B: Condens. Matter Mater. Phys.*, 2012, **85**(19), 195423, DOI: 10.1103/PhysRevB.85.195423.

66 Y. Wu, *et al.*, Facile fabrication of microfluidic surface-enhanced Raman scattering devices via lift-up lithography, *R. Soc. Open Sci.*, 2018, **5**(4), 172034, DOI: 10.1098/rsos.172034.

67 T. Tabussam, *et al.*, Surface-enhanced Raman spectroscopy for studying the interaction of organometallic compound bis(1,3-dihexylimidazole-2-yl) silver(i) hexafluorophosphate (v) with the biofilm of Escherichia coli, *RSC Adv.*, 2024, **14**(10), 7112–7123, DOI: 10.1039/d3ra08667d.

68 C. Byram, J. Rathod, S. S. B. Moram, A. Mangababu and V. R. Soma, Picosecond Laser-Ablated Nanoparticles Loaded Filter Paper for SERS-Based Trace Detection of Thiram, 1,3,5-Trinitroperhydro-1,3,5-triazine (RDX), and

Nile Blue, *Nanomaterials*, 2022, **12**(13), 2150, DOI: 10.3390/nano12132150.

69 H. J. Koster, H. J. O'Toole, K. L. Chiu, T. Rojalin and R. P. Carney, Homogenous high enhancement surface-enhanced Raman scattering (SERS) substrates by simple hierarchical tuning of gold nanofoams, *Colloids Interface Sci. Commun.*, 2022, **47**, 100596, DOI: 10.1016/j.colcom.2022.100596.

70 Y. Rajesh, M. S. S. Bharati, S. V. Rao and M. G. Krishna, ZnO nanowire arrays decorated with titanium nitride nanoparticles as surface-enhanced Raman scattering substrates, *Appl. Phys. A: Mater. Sci. Process.*, 2021, **127**(4), 270, DOI: 10.1007/s00339-021-04424-w.

71 L. Yang, *et al.*, A Ag synchronously deposited and doped TiO2 hybrid as an ultrasensitive SERS substrate: A multifunctional platform for SERS detection and photocatalytic degradation, *Phys. Chem. Chem. Phys.*, 2018, **20**(22), 15149–15157, DOI: 10.1039/c8cp01680a.

72 Y. Chen, Y. Hu and G. Li, A Review on Non-Noble Metal Substrates for Surface-Enhanced Raman Scattering Detection, *Chemosensors*, 2023, **11**(8), 427, DOI: 10.3390/chemosensors11080427.

73 Y. Wang, W. Ruan, J. Zhang, B. Yang, W. Xu, B. Zhao and J. R. Lombardi, Direct observation of surface-enhanced Raman scattering in ZnO nanocrystals, *J. Raman Spectrosc.*, 2009, **40**(8), 1072–1077, DOI: 10.1002/jrs.2241.

74 X. Xue, W. Ji, Z. Mao, Y. Wang, X. Wang, W. Ruan, B. Zhao and J. R. Lombardi, Raman investigation of nanosized TiO2: effect of crystallite size and quantum confinement, *J. Phys. Chem. C*, 2012, **116**(15), 8792–8797, DOI: 10.1021/jp2122196.

75 Y. Wang, H. Hu, S. Jing, Y. Wang, Z. Sun, B. Zhao, C. Zhao and J. R. Lombardi, Enhanced Raman scattering as a probe for 4-mercaptopyridine surface-modified copper oxide nanocrystals, *Anal. Sci.*, 2007, **23**(7), 787–791, DOI: 10.2116/analsci.23.787.